52nd AIAA/SAE/ASEE Joint Propulsion Conference
Salt Lake City UT, 25-27 July 2016

Throttled Launch-Assist Hybrid Rocket Motor for a Towed Glider Air Launch Vehicle.

Zachary S. Spurrier, Sean D. Walker, Stephen L. Merkley, Graduate Research Associates

and

Stephen A. Whitmore, Professor

Mechanical and Aerospace Engineering (MAE) Department
Utah State University, UMC 4130,
4130 Old Main Hill
Logan Utah, 84322-4130

June 9, 2016

This document details the design, integration, and testing of a throttled launch assist hybrid rocket motor for an airborne nano-launch platform. Gaseous oxygen and additively-manufactured ABS are used as the propellants. This study establishes the requirements for this launch assist propulsion system, develops the system design features, and develops a closed-loop proportional throttle control law. The detailed end-to-end system design is presented. Initial static tests were performed with a cylindrical fuel port to verify system functionality and establish a baseline for the propellant regression rate and optimal O/F ratio. Subsequent tests are performed using a helical fuel port to increase the volumetric efficiency of the system and allow operation near the optimal O/F condition. Multiple restarts of each system configuration are demonstrated. Results of both open- and closed loop throttle tests are presented.

I. Introduction

Since the early days of spaceflight an unachieved goal has been to create an orbital launch system capable of operating from runways with convenience and flexibility similar to aircraft. Due mainly to propulsion technology limitations with chemical rocket engines, nearly all launch systems developed to date perform takeoff vertically from specialized launch pads and have very limited operational flexibility. Fixed-base launches are restricted to certain azimuths and orbit inclinations (depending on launch site) and launch windows are typically short in duration and infrequent in occurrence.

A recent NASA-DARPA[i] study has concluded that there exists a significant potential for horizontal air-launch to provide critical strategic advantages and "assured" access to space when compared to fixed base launch operations. Because the launch altitude and airspeed are achieved using a high-efficiency air-breathing propulsion system, there is a significant reduction in the required ΔV that must be delivered by the launch vehicle, and a significantly smaller launch vehicle is allowed. The study concludes that a performance boost to orbit of 50% may be obtainable. An air launched vehicle can also achieve a wide range launch inclinations and right ascensions from a single deployment site. Launches performed at or near the equator can be accomplished with a 12% to 25% reduction in propellant mass. More importantly, air-launch provides a wide range of

operational options including on-demand launch azimuth, flexible launch windows, and nearly all-weather launch opportunities. This capability enhancement can lead to increased launch rates and an associated overall launch-cost reduction.

A. Towed-Glider Air Launch System (TGALS).

The DARPA/NASA study concluded that a towed, remotely-piloted, unpowered glider bottom-launching a space-launch vehicle has the potential to be significantly smaller and operationally cheaper than a dedicated human-crewed carrier aircraft. Because the towed platform is separated from the launch vehicle by a significant distance, the risk to human crew is significantly reduced. Consequently, the launch platform does not require certification for human occupancy.

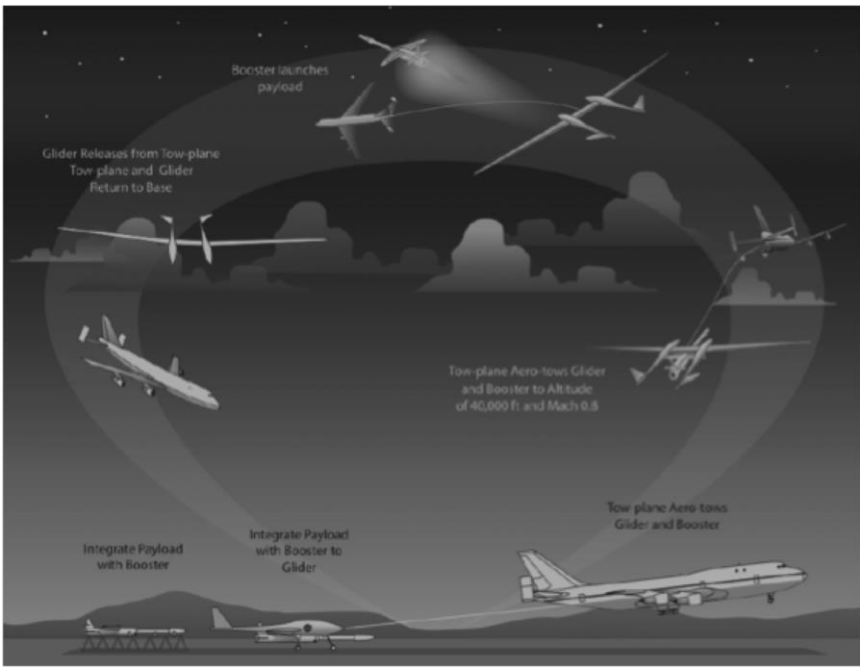

Figure 1. CONOPS of Towed-Glider Air Launch System.

The high L/D towed platform offers the potential for a significantly increased operational range when compared to a coupled launch vehicle and lift platform. Finally, the glider platform can be towed to the launch altitude using a variety of options, this concept offers a significant increase in operational flexibility. These features offer the potential to dramatically lower launch operating costs. Such cost savings could represent a market-disruptive potential for the emerging commercial spaceflight industry. Figure 1 shows the Concept of Operations (CONOPS) for a TGALS operational platform.

B. AFRC Demonstration Prototype of Towed-Glider Air Launch System (TGALS).

Previous air-launch studies[ii,iii,iv] have demonstrated that a key parameter for optimal air-launch trajectories is the launch flight path angle. Conceptually, an optimal air launch flight path angle at the launch altitude and airspeed would place the launch vehicle onto the trajectory follows the optimal ground launch trajectory. The glider platform itself is unable to achieve this flight condition, and launch assist propulsion is required. Currently, AFRC is developing a prototype platform to verify the operational feasibility of the towed-launch platform concept. A primary objective of this demonstration project is to tow to altitude, release, and safely return to base with an instrumented, sub-scale, remotely piloted, twin-fuselage glider with a representative scaled small-rocket system. Figure 2 shows a photograph of the demonstration vehicle scaled-prototype. The launch vehicle is attached to the center-pylon of the launch platform. This demonstration

project will allow AFRC to gain operational experience with the towed-glider platform, understand aerodynamic and structural interactions of the rocket and pylon, and demonstrate that the launch platform can achieve the proper launch attitude.

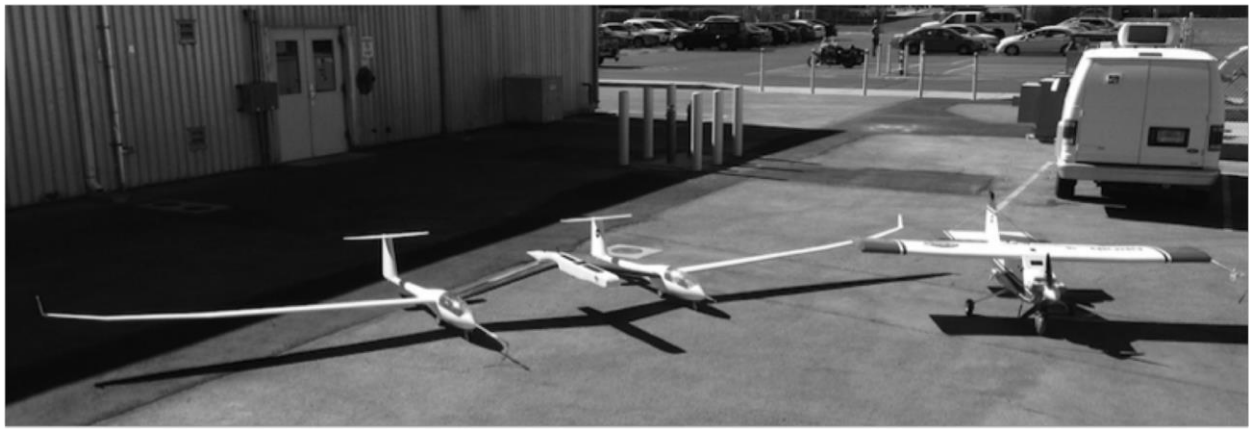

Figure 2. Demonstration Prototype of Towed-Air Launch Platform.

C. Top-Level Requirements for Launch Assist Rocket System.

Based on a preliminary analysis performed by NASA AFRC, the top-level system requirements for the launch-assist propulsion system are

1. Maximum thrust of *200 lbf.*
2. Capability to throttle from < *20% to 100%. Simulation studies verified that a high level of system thottleablilty was necessary to achieve the required flight profiles.*
3. Provide sufficient throttle fidelity to allow a *2-2.5 g* pullup to 70^{o} flight path angle at *85 knots true airspeed (KTAS)* at 4500 ft above mean sea level (MSL).
4. Provide sufficient impulse to allow the launch platform to hold the 70^{o} flight path angle for a minimum of 5 seconds.
5. Use non-toxic, non-explosive propellants, and a non-pyrotechnic ignition system.
6. A properly engineered, restartable launch vehicle. "Stage 0" trajectory should retain sufficient impulse allow contingency energy management for the glider launch platform to return to base. Thus, system restartability is highly desirable.

Multiple options are available to achieve the required launch-assist total impulse, including a small solid rocket booster, a bi-propellant liquid system, a cold-gas system, a mono-propellant hydrazine system, and a hybrid rocket system. The bi-propellant liquid rocket was discarded due to the associated complexity and expense of engineering the required sub-systems. The hydrazine system was discarded because of the potential vapor hazard and the associated operational complexities of working with a toxic propellant. The solid rocket booster, although offering a simple solution, does not deliver the impulse precision and variable thrust required to place the launch platform onto the proper launch attitude. Finally, because of the associated low specific impulse *(I_{sp}),* the cold gas system required more propellant than can be carried by the launch platform with the launch vehicle payload. Thus, by process of elimination a hybrid system was selected for the launch-assist propulsion unit (LAPU).

II. TGALS Launch Assist Propulsion Unit (LAPU) System Design Overview

Figure 3 presents a top-level solid-model schematic of the Launch Assist Propulsion (LAPU) Systems. The prototype system is based on a previous design tested at Utah State University.[v] Pictured are the gaseous oxygen (GOX) oxidizer tanks, the high pressure fill and relief valves, a tank manifold, a manually-set pressure reducing regulator, a low-pressure burst safety disk, an electronic run-valve, a ball-type throttle valve, the electrical valve actuator, and the motor thrust chamber and pressure case. The associated pneumatic assembly piping and connectors are also shown. Major features are described in detail in the following subsections.

D. Hybrid Motor Combustion Chamber and Ignition System.

The hybrid motor system employs gaseous oxygen (*GOX*) as the oxidizing agent and additively-manufactured acrylonitrile-butadiene-styrene (*ABS*) as the fuel component. These propellants are non-explosive, non-toxic, and remain inert until combined within the motor combustion chamber. The fuel grain is manufactured using the conventional fused deposition modeling (FDM) technique of additive manufacturing for thermo-plastics, and features "snap-together" interlocks that allow the grain segments to be manufactured separately and then assembled for use. The FDM processed grain segments also allow for an embedded helical fuel port that enhances the fuel burn rate and combustion efficiency.

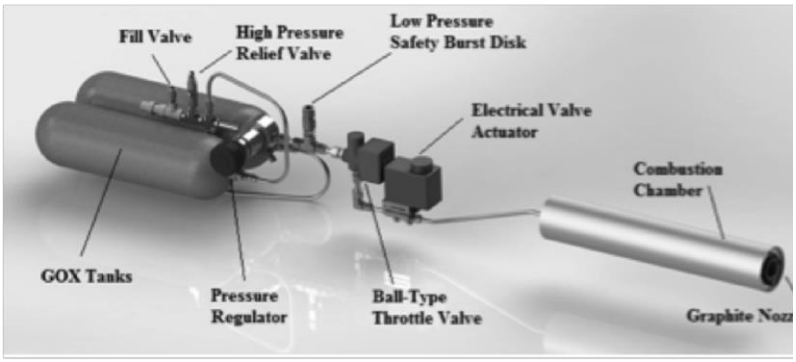

Figure 3. Top-Level Schematic of LAPU Hybrid Motor System Components.

Figure 3 shows a cut-away schematic for the hybrid rocket motor case. Pictured are the helical fuel grain interlocks, injector cap with ignition electrodes, and post-combustion chamber with graphite nozzle insert and adapter. The motor case is constructed from a modified Cessaroni solid rocket motor case, and is 98 mm in diameter and approximately 70 cm long. The pictured fuel grain is additively manufactured from commercially-available Stratasys ABSplus-340® feed-stock.[1] Table 1 lists dimensions and weights of the major thrust chamber system components.

The system is ignited using a patent pending arc-ignition technology developed at Utah State University.[vi] This technology exploits the unique electrical breakdown properties of additively-manufactured ABS to allow on-demand start and restart. The non-pyrotechnic system requires two independent signals to initiate combustion and is thus duel redundant to the Hazards of Electromagnetic Radiation to Ordnance (HERO) as defined by MIL-STD-464.[vii] Figure 3 shows a schematic for the hybrid motor case, the helical fuel grain interlocks, injector cap with ignition electrodes, and post-combustion chamber with graphite nozzle are shown. The oxidizer injector consists of a single port injector with a .402 cm^2 area in order to allow the required mass flow of at *least 250 g/sec (0.55 lbm/sec)* into the combustion chamber without choking. The ignition

[1] *www.stratasys.com/materials/fdm/absplus/*

power-processing-unit (PPU) and oxidizer delivery system are not shown in Figure 3. The ground test motor systems are designed to reproduce the flight systems as closely as possible.

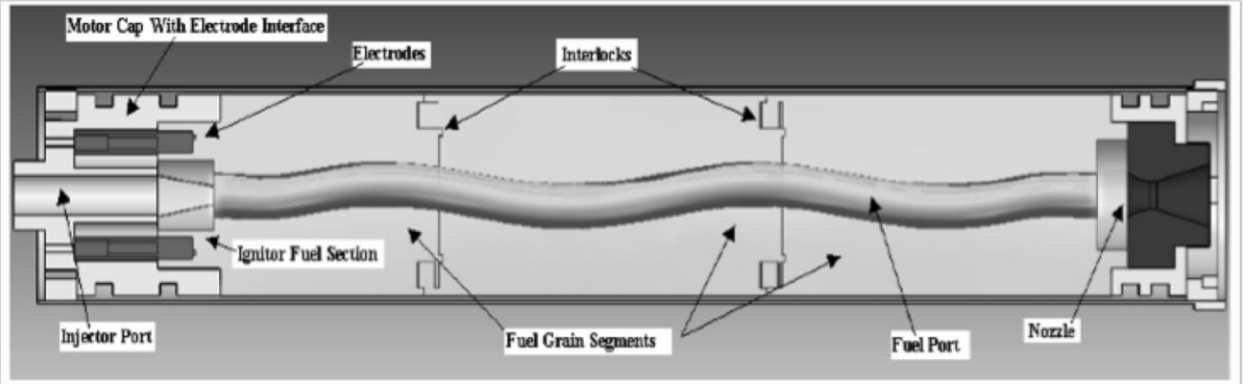

Figure 3. Schematic of LAPU Hybrid Motor with Snap-Together Helical Segments.

Table 1. Thrust Chamber Component Dimensions and Weights.

Motor Case	**Length:** 27.73 in. (70.2 cm)	**Diameter:** 3.86 in. (98 mm)	**Empty Weight:** 7.95 lbm (3.61 kg)	**Total Loaded Motor Weight:** 14.41 lbm (6.54 kg)
Injector	**Diameter:** 0.282 in. (0.716 cm)	**Type:** Single port, aluminum	**Discharge Area:** .0623 in^2 (.402 cm^2) Cd ~ 0.85	**Total Oxidizer Load:** 11.2 lbm (3.8 kg)
Machined graphite nozzle	**Diameter:** 0.728 in. (1.85 cm)	**Expansion Ratio:** 4.65	**Conical exit angle:** 15 deg.	**Throat Erosion Rate:** 0.011 cm/sec
ABS Fuel grain	**Length:** 23.08 in. (58.61 cm) **Diameter:** 3.31 in. (8.4 cm)	**Initial Port Diameter:** 0.9 in. (2.286 cm)	**Fuel Weight:** 6.462 lbm (2.932 kg)	**Helix Ratio:** 0.5:1 **Pitch Length:** 7.69 in. (19.5 cm) (3 turns)

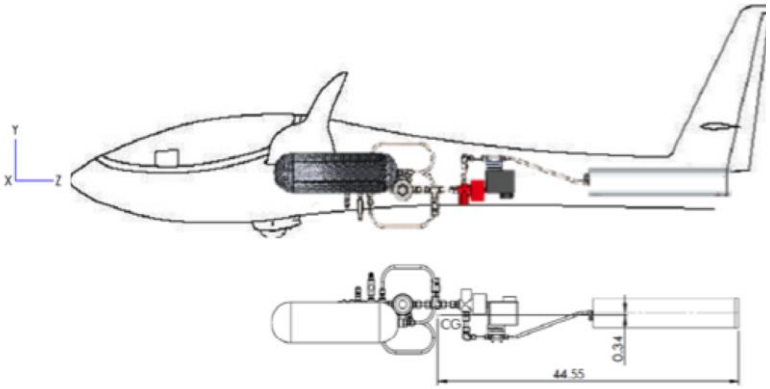

Figure 4. Installed LAPU System Schematic.

Figure 4 shows the flight system components in the approximate the flight orientation, as mounted to the pylon between the twin vehicle fuselages. The fully loaded system weight is approximately 23.9 kg (52.6 lbm), and is approximately 165 cm (65 in.) in end-to-end length. Each GOX tank is rated for a 4500 psig maximum fill capacity, and holds approximately 1.93 kg (4.24 lbm) of oxidizer when filled at room temperature. The motor dry system weight is approximately 18 kg (40.3 lbm).

E. Flight Test Oxidizer Delivery System.

Figure 5 presents the oxidizer delivery system piping and instrumentation diagram (P&ID) for the flight test system. The system is designed to operate between 4500-to-1500 psig upstream of the pressure regulator, and between 750-to-800 psig downstream of the regulator. Required safety-of-flight system instrumentation consists of pressure transducers upstream of the regulator and a chamber pressure transducer. The oxidizer delivery system components consist of

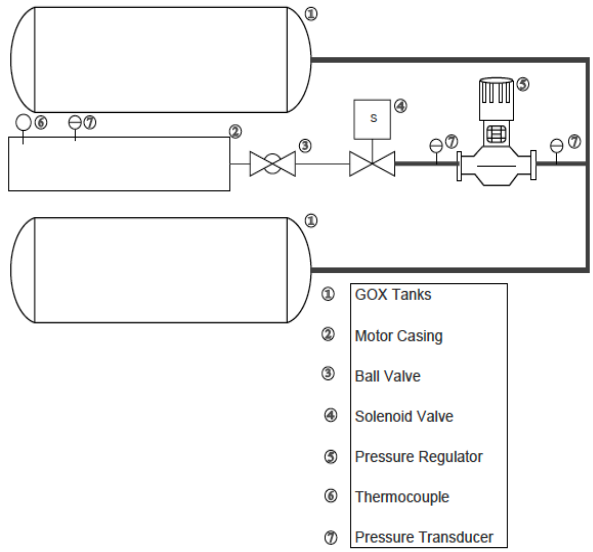

Figure 5. Flight Vehicle Oxidizer Delivery System P&ID.

- Two aviation-rated *4500 psig* carbon-composite gaseous oxygen storage tanks, manifolded together.
- A manual set pressure reducing regulator.
- ball valve.
- A DC-solenoid actuated run valve.
- An electronically actuated throttle
- The thrust chamber injector.

The throttle ball-valve allows the system to regulate the mass flow by adjusting the outlet flow coefficient (*Cv).* A full-open valve *Cv* range of approximately *2.5* is required to achieve the desired *250 g/sec* maximum mass flow level at a valve inlet pressure of approximately 750 psig. The valve is actuated using an *Invensciencei01300* rotary

actuator[2]. The 12-V powered ball-valve rotary actuator features 0 to 5 VDC analog input proportional control signal.

The pressure regulator has a lockable, manual set-point. Assuming a full-filled capacity for the O_2 tanks (*4500 psig)* and the assumed ball-valve Cv (2.5), a regulator set-point range of approximately 750 *psia* will be required to achieve the prescribed maximum thrust level of approximately *200 lbf.* It is assumed that the *Cv* for the electronic run valve is greater than 2.5 in order to ensure that the flow will not choke upstream of the throttling ball valve. The regulator set point will be manually tuned to adjust for any potential losses in the system run valve. The regulator valve set point of 750 psig was selected to ensure a choking mass flow of greater than *250 g/sec* at that pressure set point.

F. Ignition System Power Processing Unit and Control System.

The ignition system PPU is based on the UltraVolt® AA-series line of high-voltage power supplies (HVPS).[viii] These HVPS units take a 24-28 VDC input and provide a current-limited (30 mA) high voltage output -- up to 1 kV. The output signal is initiated by a commanded TTL-level signal. Units with output capacities from 4-30 watts are available. Previous experience with this ignition system has demonstrated that ignition can be achieved using as little as 6 watts;[ix] however, in order to ensure guaranteed reliable motor ignition a 30-watt model will be employed for this design. Figure 6 shows the interface to the AA-series HVPS. The unit features current and high-voltage output signals that are used to monitor the system performance on the flight vehicle. The remote adjust input is set to the maximum value, and the unit output is enabled by driving the system enable pin to ground. Figure 7 shows the complete electronics interface diagram for the launch-assist motor subsystems. At this point in the design process, the complete vehicle electronics interface to the motor subsystems has not been entirely defined.

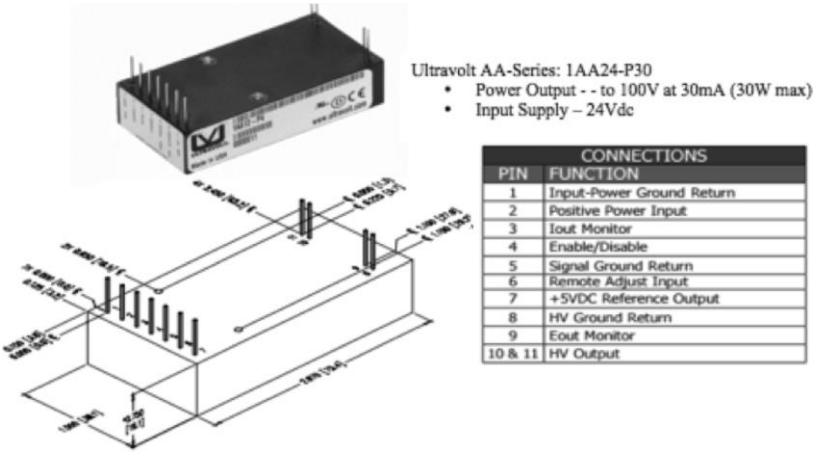

CONNECTIONS	
PIN	FUNCTION
1	Input-Power Ground Return
2	Positive Power Input
3	Iout Monitor
4	Enable/Disable
5	Signal Ground Return
6	Remote Adjust Input
7	+5VDC Reference Output
8	HV Ground Return
9	Eout Monitor
10 & 11	HV Output

Figure 6. Schematic of the UltraVolt HVPS System Pinouts and Interface.

[2] http://www.invenscience.com/index_files/torxis_rotary_servo.htm/

III. Ground Test System Overview

The ground test system used to perform the preliminary integration and qualification tests on the LAPU subsystems employs a more extensive instrumentation suite including an in-line Venturi flow meter on the oxidizer feed line downstream of the pressure regulator, and multiple thermocouples to monitor the system temperatures at various points. The system is integrated onto a portable test cart with all hot fire testing performed in the Propulsion Research Laboratory's on-campus test cell. Figure 8 shows the ground test cart. Figure 9 shows the piping and instrumentation test schematic for the ground test system. The ground test system is operated using a National Instruments USB-based *NI cDAQ-9174* Data Acquisition and Control Unit[3] with data logging and system control performed via a LabVIEW interface program.

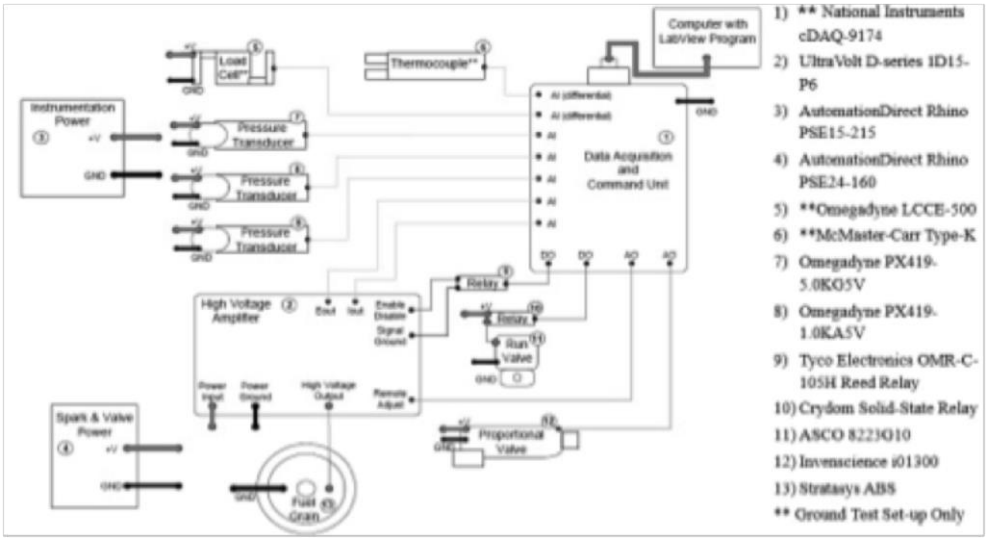

Figure 7. Launch-Assist Motor Systems Electronics Interface Diagram.

[3] http://sine.ni.com/nips/cds/view/p/lang/en/nid/207535/

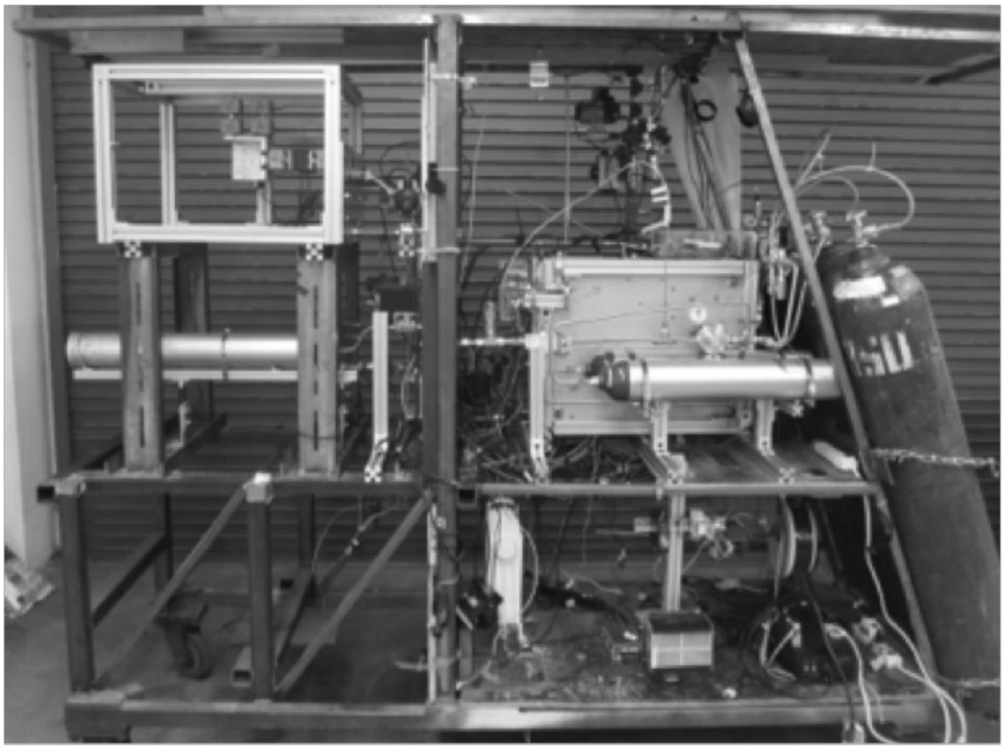

Figure 8. Ground Test Cart for TGALS LAPU Verification Testing.

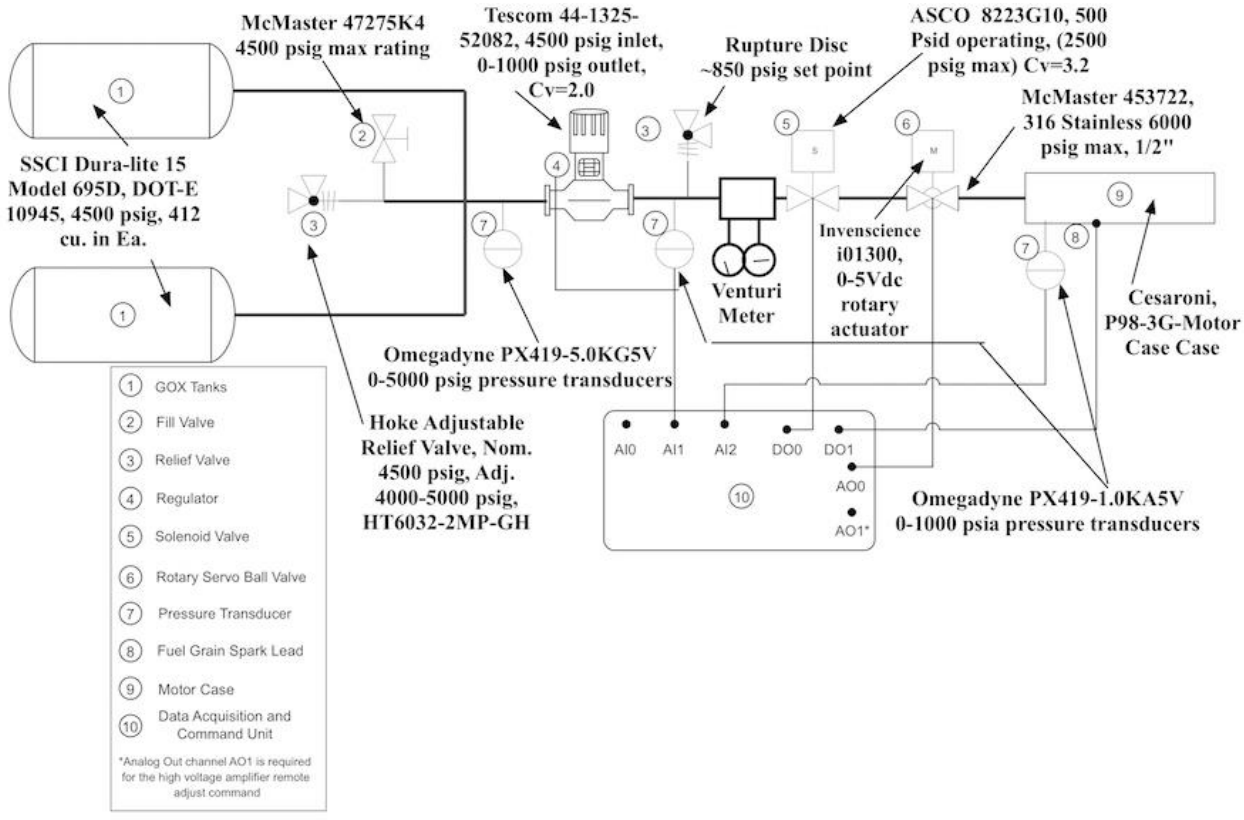

Figure 9. Ground Test Motor Systems P&ID.

IV. Ground Test Results

A series of ground development tests using three different configurations were performed. Two sets of static fire tests were performed to verify the throttle capability of the system. Following these tests, several throttled tests were performed to characterize system response. Using the characterization data, a simulation was built to determine the optimal controller settings for matching a given thrust profile. From the optimal controller settings, a final hot fire burn was performed to verify the simulation and system response.

G. Cylindrical Port Hot Fire Tests.

The first series of tests ground tests were performed using an existing ABS fuel grain left over from earlier *nitrous oxide (N_2O)/ABS* testing campaign of Whitmore and Peterson.[x] Stratasys, Inc printed this fuel grain as a single monolithic piece with a density of *0.975 g/cm^3* using a Fortus 900mc production FDM machine.[4] This series of 5 tests were performed at the full throttle position with the ball valve set in the full opening position. Following each test, the motor fuel grain was removed from the motor case and the consumed fuel mass was measured.

Figure 10 plots the measured resulting regression rates as a function of the oxidizer mass flux. (G_{ox}). For these calculations the oxidizer mass flow was measured using an in-line calibrated Venturi mass flow meter. The fuel mass flow was calculated as the difference between the measured oxidizer mass flow and the nozzle exit mass flow. The nozzle exit mass flow was calculated based on the measured chamber pressure P_0, nozzle exit area A^*, and exhaust gas properties using the 1-dimensional De laval choking mass flow equation.[xi]

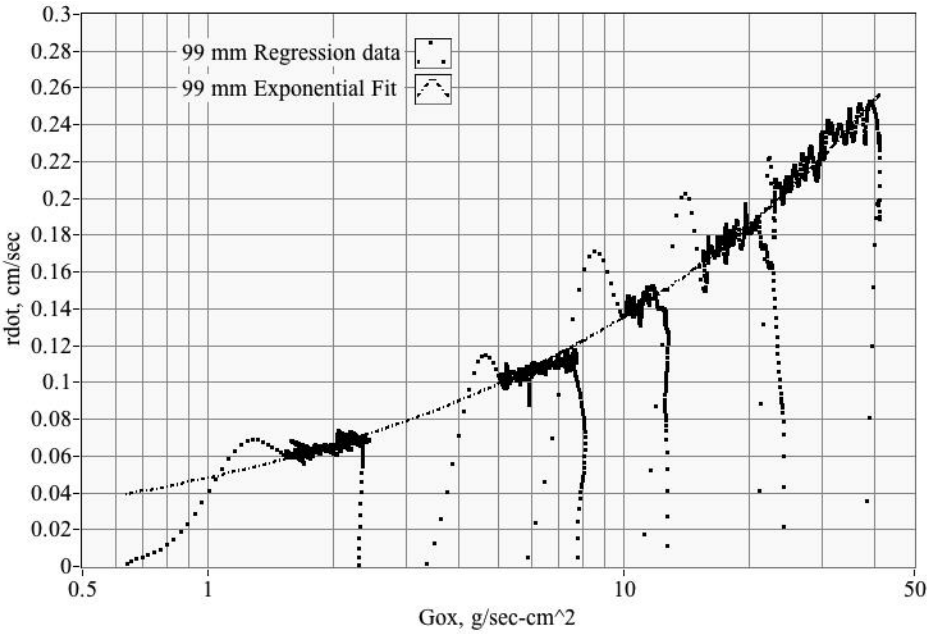

Figure 10. Regression Rate for GOX/ABS Cylindrical Port Tests.

The combustion products for the combustion flame temperature T_0, gas-specific constant R_g, and ratio of specific heats γ, were calculated using tables developed using the NASA chemical equilibrium program "Chemical Equilibrium with Applications," (CEA).[xii] For the CEA calculation the measured chamber pressure was used as an input, and the O/F ratio entered into CEA was adjusted to produce a fuel mass flow whose integral value exactly equaled the consumed fuel mass measured after each test.

[4] http://www.stratasys.com/3d-printers/production-series/fortus-900mc/

Figure 10 also plots an exponential curve fit of the form

$$\dot{r}_L = a \cdot G_{ox}^{\ n}, \tag{1}$$

where, $\dot{r}_L$ is the mean longitudinal regression rate, *{a}* is the scale factor, G_{ox} is the oxidizer mass flux, {*n* } is the burn exponent. For a cylindrical fuel port, it can be shown that the oxidizer-to-fuel mass flow ratio (*O/F*) at any burn time is

$$O/F = \frac{1}{4^n \cdot \pi^{1-n}} \frac{\dot{m}_{ox}^{\ 1-n} \cdot D_{port}^{\ 2n-1}}{a \cdot \rho_{fuel} \cdot L}. \tag{2}$$

Analysis of Eq. (2) shows that when the burn exponent is {*n > 1/2*}, the *O/F* ratio is progressive and increases as the fuel grain burns and the port opens up. Conversely, when {*n < 1/2}* the *O/F* burn is regressive and becomes increasingly rich with time, and {*n = 1/2*} the burn rate is neutral and implies no *O/F* shift during the burn. The majority of commonly used oxidizer/fuel combinations (including *N_2O/ABS*) have burn exponents greater than *1/2*, and thus burn increasing leaner with time.[xiii]

For the GOX/ABS grain cylindrical fuel port tests, the resulting best-fit burn parameters are

$$\begin{bmatrix} a \\ n \end{bmatrix} = \begin{bmatrix} 0.048 \dfrac{cm^{1+2n}}{g - s^{1-n}} \\ 0.45 \end{bmatrix}. \tag{3}$$

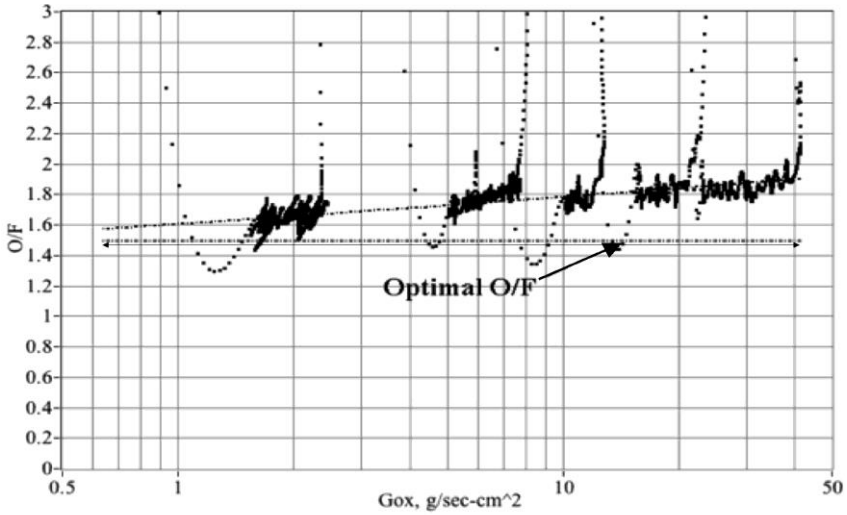

Figure 11. Oxidizer-to-Fuel Shift of Cylindrical ABS Fuel Port.

The value for the burn exponent {*n=0.450}* is considerably smaller than the value measured by Ref. (x), {*n~0.762*}. The derived burn exponent suggests that the LAPU motor should exhibit very little O/F shift during the burn. Figure 11 verifies this assertion where O/F is plotted as a function of oxidizer mass flux. The *O/F* shift is slightly regressive with the motor burning only slightly richer as the fuel port opens up. This quantitative behavior matches the qualitative physical observations of the various motor burns. The larger 98-mm motor plume was observed to show very little change in the plume characteristics during the fuel grain burn lifetime -- approximate 20 seconds.

H. B. Helical Port Static Tests

Measuring the Required Regulator Set Point

As shown by Fig. (11) the O/F ratios for the cylindrical port fuel grain lies just above the optimal operating value of approximately 1.5 for GOX/ABS (Ref. [v]). Thus for the second series of tests a moderate helix was printed into the fuel grain to lower the mean O/F ratio. As listed in Table 1, the port helix radius was 1/2 of the initial fuel port diameter. The helix pitch length was 19.5 cm (7.68 in.) resulting in 3 complete turns along the fuel port length. This change was incorporated to slightly lower the O/F ratio so that the motor would burn nearer the optimal operating condition. The grain was printed as three interlocking segments on the MAE department's Dimension 1200es[5] using ABSplus-340 feedstock. In addition to the modification of the fuel port, the nozzle retainer exhibited unwanted erosion, and a small redesign was made to reduce the erosion potential.

The testing campaign on the helical fuel port motor was broken into two sets. A primary function of the first test set was to measure the necessary regulator set point to achieve the full required 200 lbf thrust level. A series of 4, 2-second burns at various regulator set points were performed to determine the required level set pressure level. The regulator output "droop" was found to be strongly a function of oxidizer massflow. Figure 12 plots these results. Fig. 12a plots regulator output from the set point (droop) as a function of the oxidizer massflow, and Fig. 12b plots the achieved output pressure as a function of the regulator set point. The result is that the achieved full-open thrust and chamber pressure are also strongly a function of the regulator set point. Thrust coefficient is also strongly influenced by the regulator set point. Figure 13 plots this result. With the throttle ball-valve fully open, the full required thrust level of 200 lbf mandates a regulator set point of at least 750 psig.

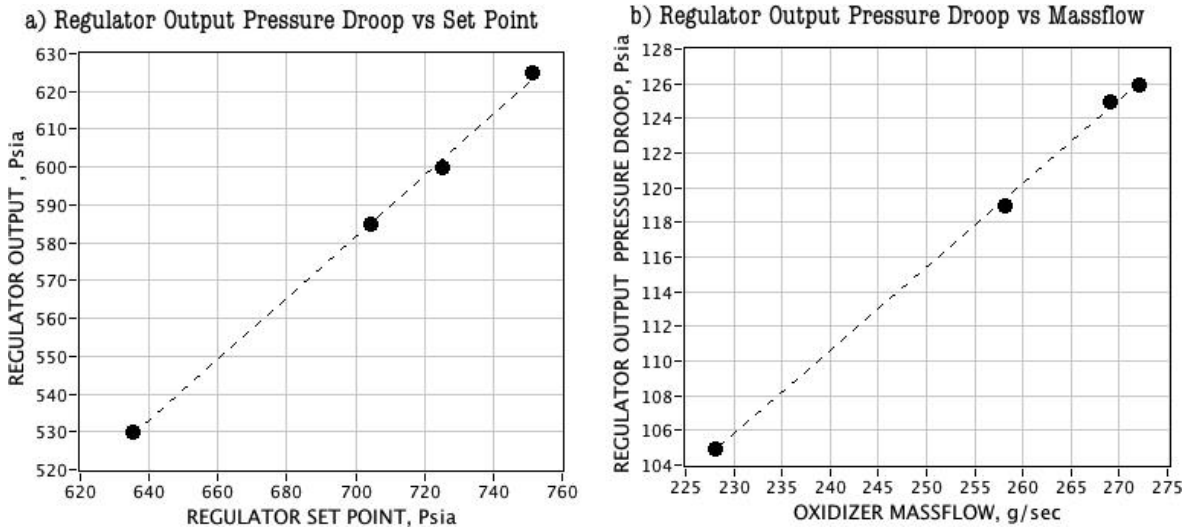

Figure 12. Regulator Output Droop as a Function of Oxidizer Massflow Set Point.

[5] http://www.stratasys.com/3d-printers/design-series/dimension-1200es/

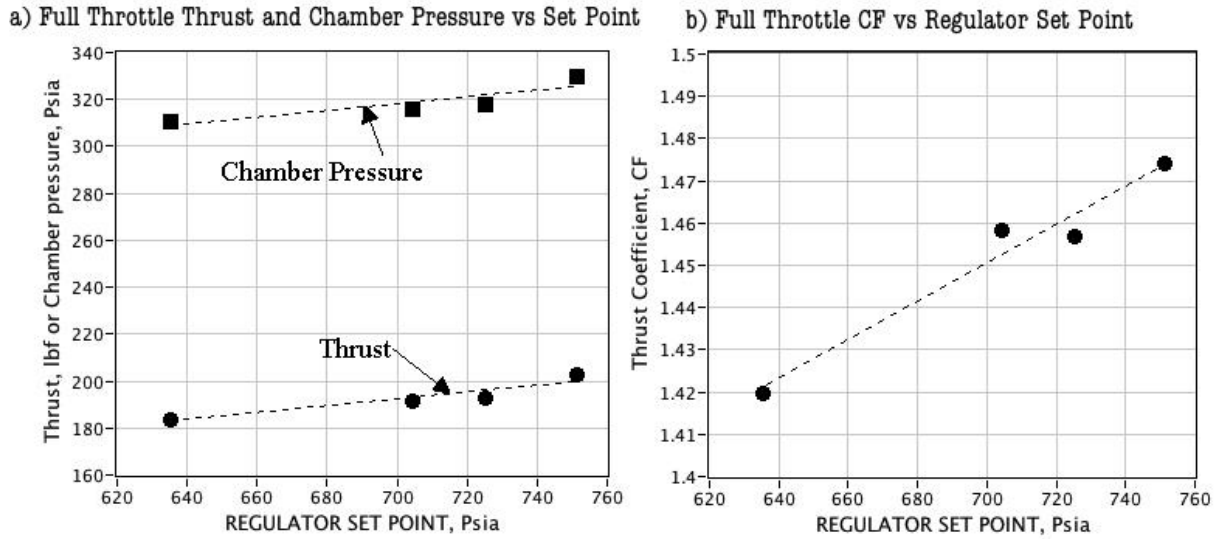

Figure 13. Full Throttle Thrust Chamber Pressure, and Thrust Coefficient as a Function of Regulator Set Point.

Oxidizer-to-Fuel Ratio for the Helical Fuel Port.

The initial tests of the helical fuel port were also used to verify that the changes to the grain configuration moved the *O/F* ratio to the optimal operating range. Figure 14 presents these results. Here Figure 14a plots the mean *O/F* ratio for each burn is plotted as a function of the accumulated burn time on the motor. The resulting *O/F* range -- between 1.25 and 1.67 -- is overlaid onto the characteristic velocity plot C^* on Figure 14b. Here the achieved *O/F* range brackets the optimal performance range, thereby verifying the helix grain design.

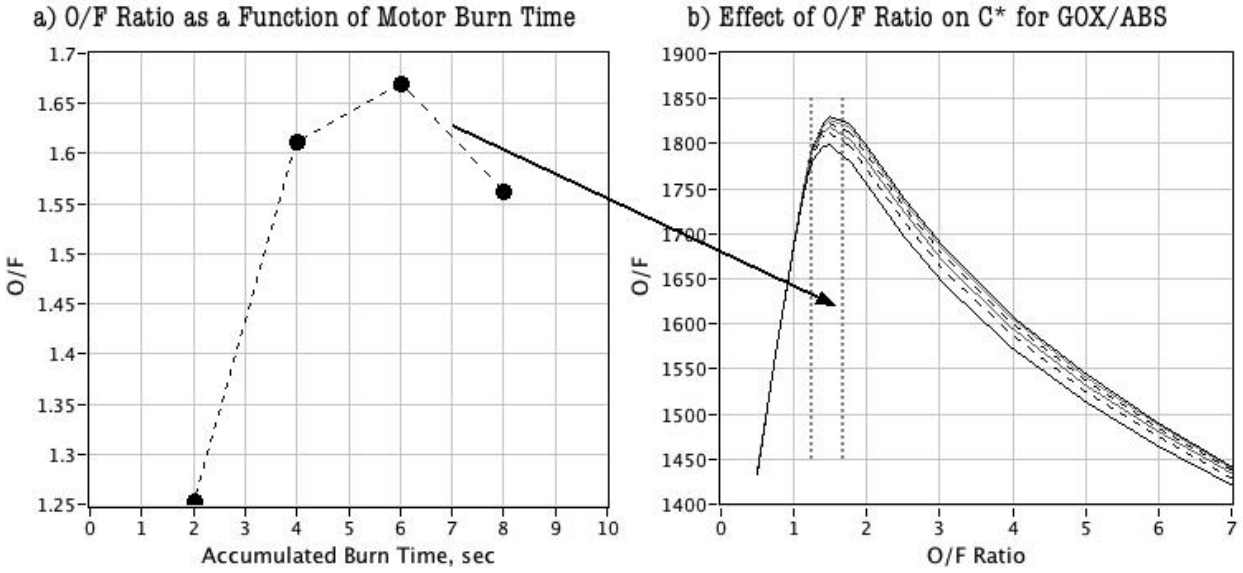

Figure 14. Achieved O/F Range for Helical Fuel Port Burn at Near Full Throttle and the resulting Effect *on C.**

Figure 15 compares the achieved C* calculated by

$$C^*_{measured} = \frac{P_0 \cdot A^*}{\dot{m}_{total}}, \quad (4)$$

against the 100% combustion efficiency theoretical values for the O/F levels of Figure 14. Figure 15 also plots the measured combustion efficiency and specific impulse, I_{sp}. The achieved combustion efficiencies, as calculated by Eq. 5, are slightly less than 80%.

$$\eta^* = \frac{C^*_{measured}}{C^*_{theoretical}}. \quad (5)$$

The low observed combustion efficiency is also reflected by the measured specific impulse of the system; which at a value of $I_{sp}=205$ seconds, is approximately 10% lower than predicted. The small drop in C* is a result of a slight observed nozzle erosion during the 8-seconds of burn time. The reasons for the low observed performance levels have yet to be determined at this point. Two causes currently being investigated include an incompletely cured printed fuel grain, and potential blow-by at the phenolic liner/graphite nozzle interface.

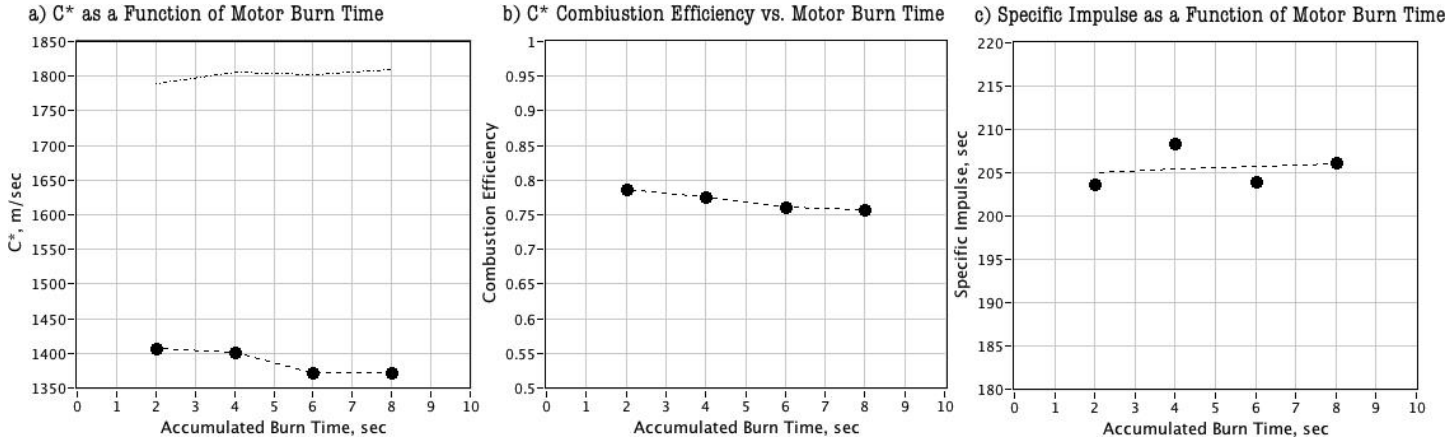

Figure 15. Cstar, Combustion Efficiency, and I_{sp} as a Function of Burn Time.

Throttle Curve Evaluation

Following the initial set of tests to determine the appropriate regulator set point, a series of six static throttle burns were performed at different ball valve voltage command levels, and using a newly fabricated helical fuel grain. To ensure that the fuel grain was fully cured, the newly printed grain was placed into a vacuum chamber, and then left in front of a fan overnight before performing these tests. Each burn was set as 2 seconds in length using up approximately 12 seconds of total burn lifetime.

Figure 16 summarizes the test results where the achieved motor thrust, mass flows, chamber pressure, and thrust coefficients are plotted as a function of the commanded ball valve voltage. Figure 16a also plots the required 200 lbf thrust full-throttle level. The effective range of the ball valve servo voltage command varies from 1.25 Volts (0% throttle) to 2.3 Volts (100% Throttle).

Figures 17 and 18 plot the system performance parameters including combustion efficiency and specific impulse as a function of the commanded throttle level and the equivalent throttle actuator voltage command. At full throttle, the system achieves slightly better combustion efficiency > 80% than was observed with the previous static tests; but this combustion efficiency

and the associated specific impulse drops off significantly at the lower throttle levels. The plots of Figure 18 support the earlier assertion that the lower than predicted specific impulse for the system is a result of lowered combustion efficiency.

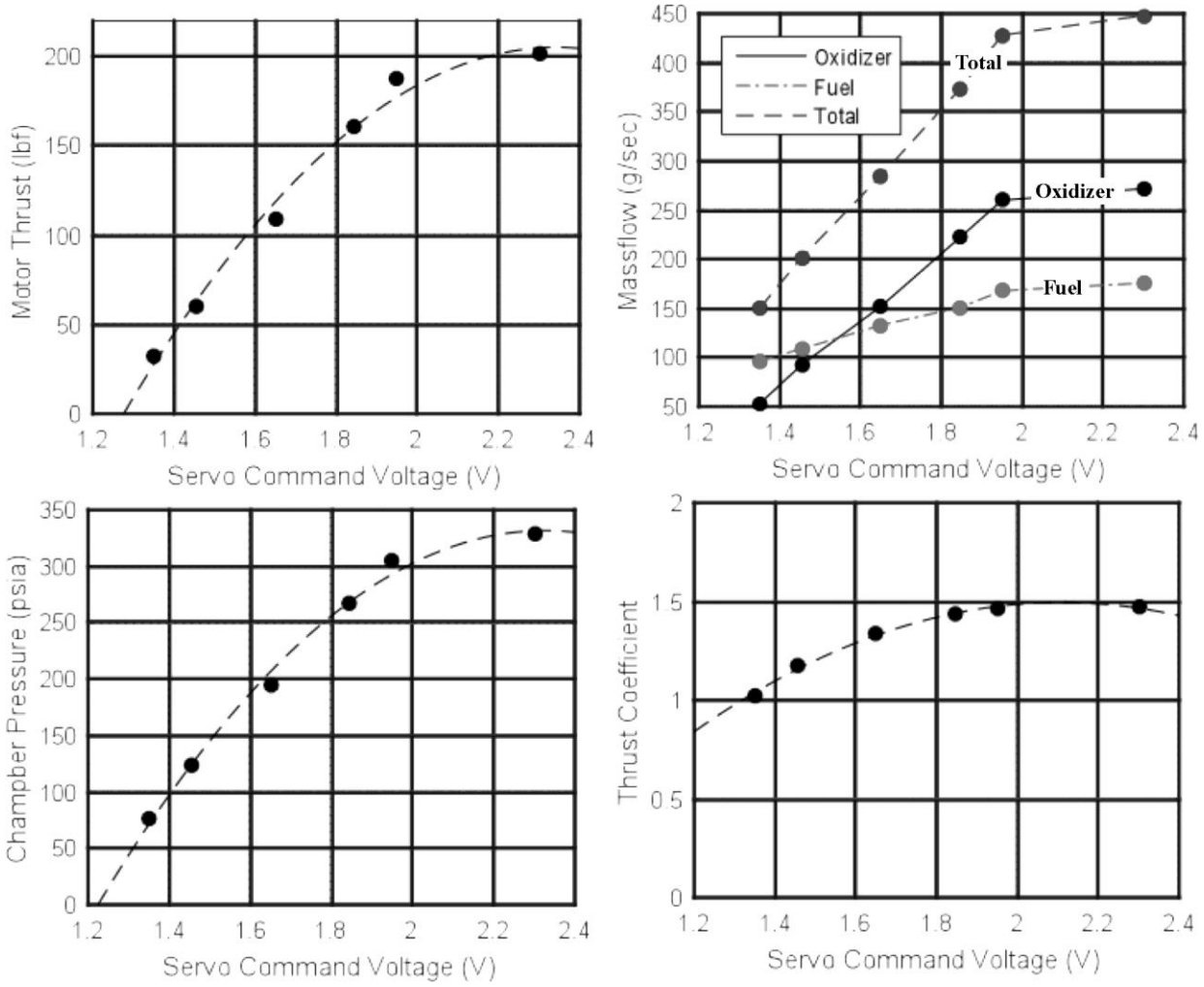

Figure 16. Helical Motor Response as Function of Commanded Ball Valve Voltage Level.

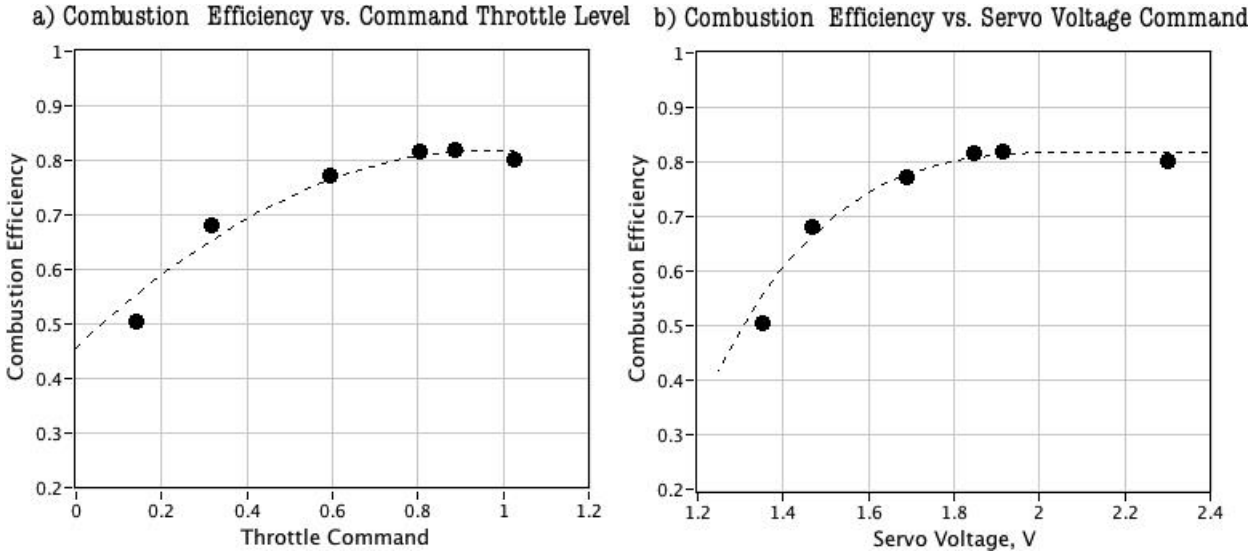

Figure 17. Combustion Efficiency as a Function of Throttle Command.

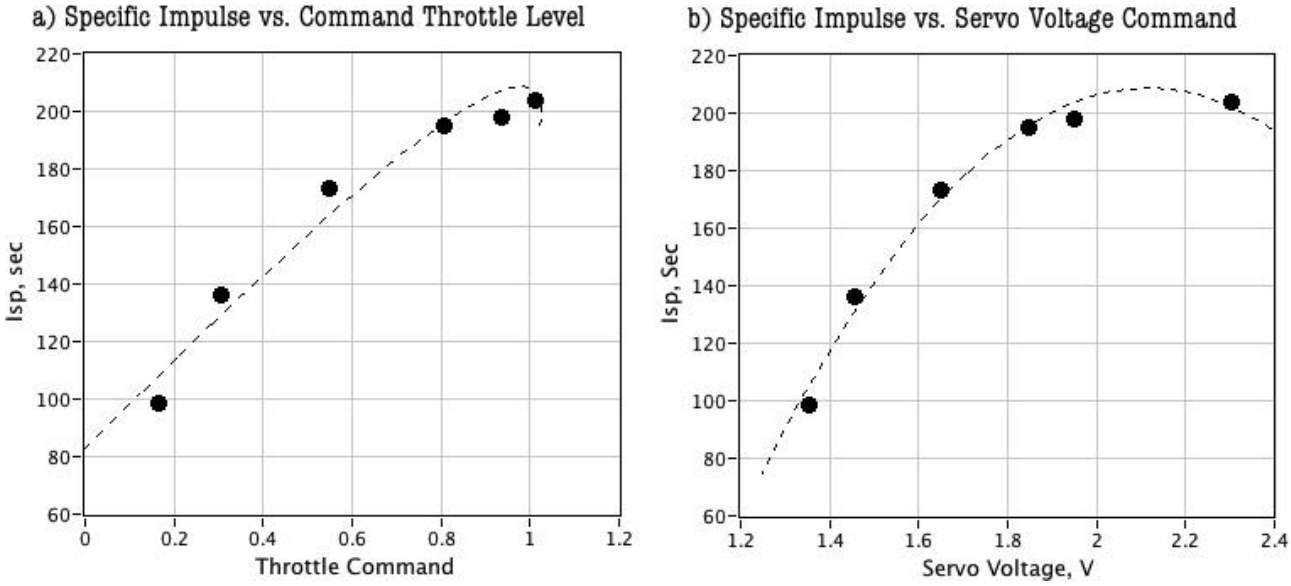

Figure 18. Specific Impulse as a Function of Throttle Command.

A. Closed Loop Throttle Testing

The results of the static throttle tests were curve fit and used to generate look-up tables that correlate the servo command voltage to motor thrust and chamber pressure to motor thrust. Using these data tables, a proportional-gain closed-loop controller using chamber pressure feedback was developed and implemented within the LabVIEW code that resides on the controlling laptop computer. Measured feedback data and closed-loop commands are sent to and from the *NI cDAQ-9174 Data Acquisition and Control Unit* via an amplified Universal Serial Bus (USB) extension.

The flow chart in Figure 19 shows the implemented control law. The control features chamber pressure feedback with closed loop servo-voltage output commands. An option for smoothing the commanded voltage using a second order Butterworth filter is included. Options for user-

prescribed thrust profile inputs are available, including step, ramp, and pull-up push-over maneuver. Values for the proportional gain k_p and the low-pass filter cutoff frequency ω_p, are user inputs.

Figure 20 shows the result of a 4 hot-fire tests performed with various set values for k_p and ω_p. For these tests the motor was ignited with the actuator command set for the 25% thrust (50 lbf) level, and the commanded thrust was increased to 25% (100 lbf) 2 seconds into the burn. The lowest gain $k_p = 0.3$ and a command filter cutoff frequency of $\omega_p = 94$ *radians/sec* (15 hz) produced the response with the minimal overshoot. The observed response latency is primarily a function of the actuator response time.

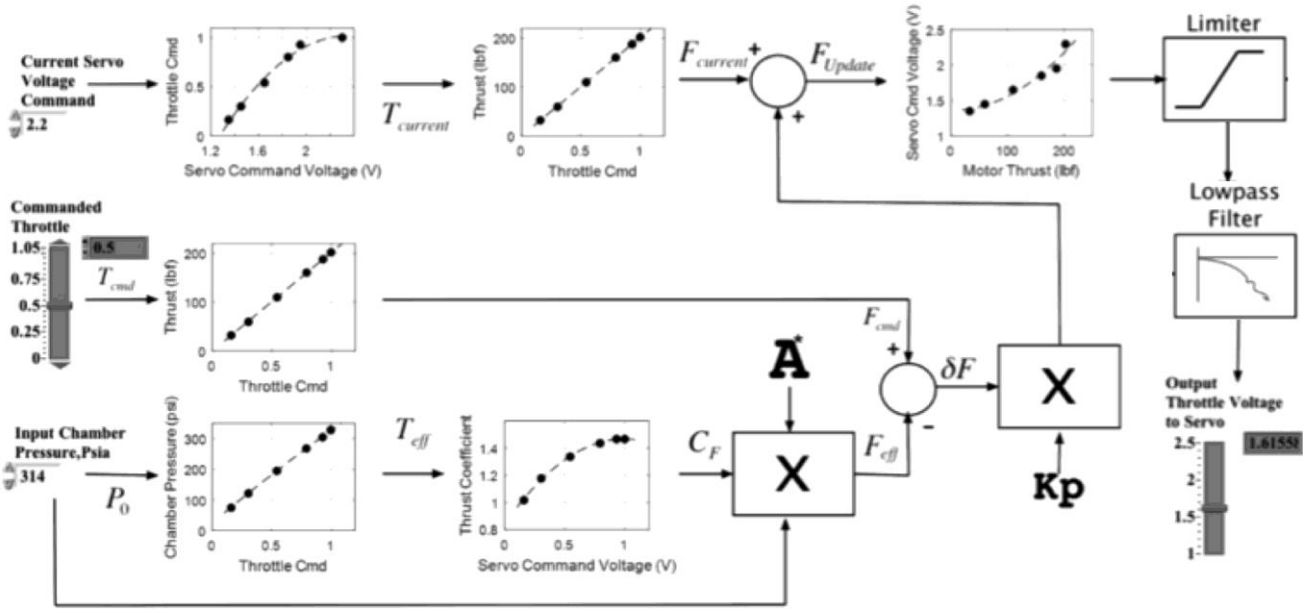

Figure 19: Proportional Closed-Loop Controller Layout.

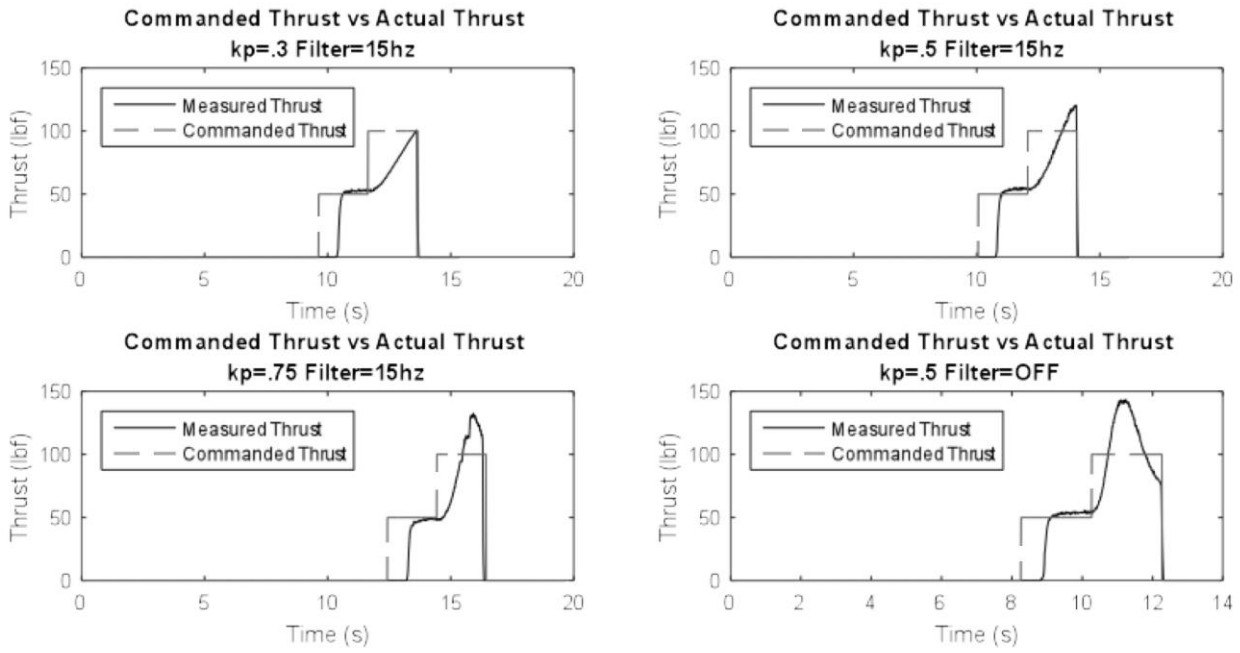

Figure 20: Thrust Profiles for Various Closed-Loop Step Tests

Closed Loop Throttle Filter Tuning

Using the controller command logic from the closed loop step tests, a simulation was designed so that ω_p and k_p can be "tuned" without requiring multiple trial-and-error hot-fire tests. The simulation decomposes the system dynamics into two concatenated components 1) a model of the servo and control ball valve dynamics, and 2) a model of the ballistic response of the motor combustion chamber. Both responses are modeled as second order transfer functions. The ball servo and ball valve transfer function is

$$\frac{\%_{MVT}}{V_{cmd}} = \frac{1}{\left(\frac{\tau_1}{2\cdot\varsigma_1}\right)^2 \cdot s^2 + \tau_1 s + 1}, \tag{6}$$

where $\{\tau_1 = 0.52\}$ and $\{\zeta_1 = 0.85\}$. These values are based on Invenscience specifications[6] for the servo response properties. In Eq. (6) $\%_{MVT}$ is the percentage of mean valve travel from fully closed t fully open -- approximately 90 degrees, and V_{cmd} is the servo command voltage level. The motor ballistics model transfer function is

$$\frac{T_{hrust}}{\%_{MVT}} = \frac{1}{\left(\frac{\tau_2}{2\cdot\varsigma_2}\right)^2 \cdot s^2 + \tau_2 s + 1}, \tag{7}$$

where the values for $\{\tau_2\}$ and $\{\zeta_2\}$ are iterated to give the best fit between the simulator and measured response. Figure 21 shows the calculation sequence that was used to estimate the best-fit transfer functions. For a given control law parameter setting for ω_p and k_p, the simulation was

[6] http://www.invenscience.com/index_files/torxis_rotary_servo.htm/

run multiple times, sweeping through the 2-dimensional parameter space for $\{\tau_2, \zeta_2\}$. In this two-dimensional parameter space, the parameter set that produces the minimum root-sum-square (RSS) error between the measured system and simulation response is selected as the "best-fit" for the motor ballistics.

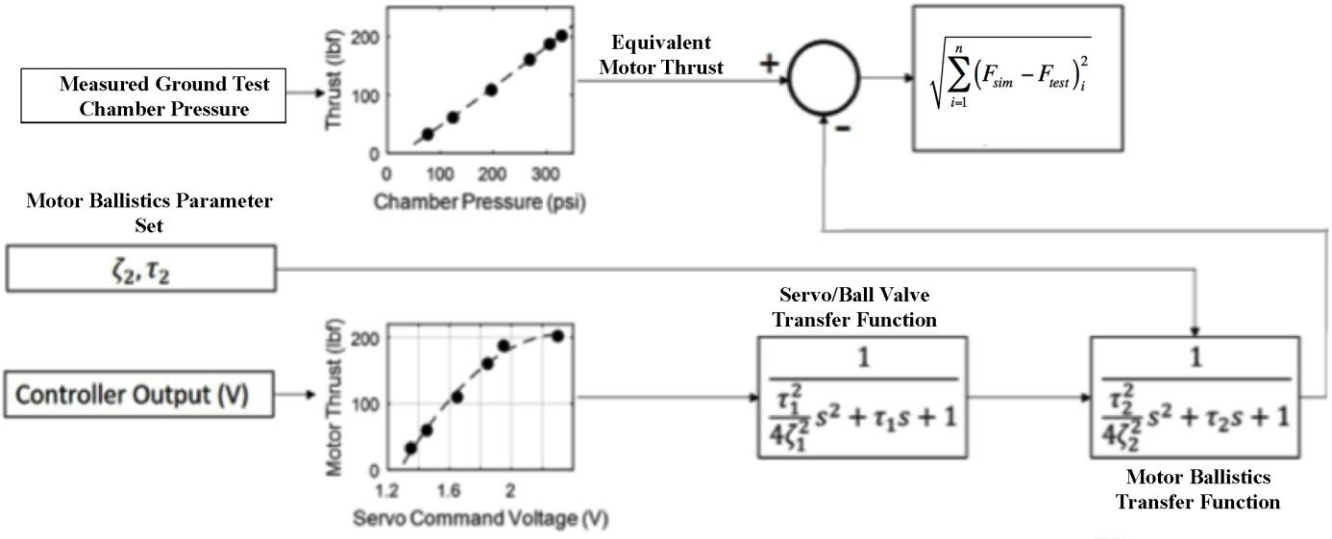

Figure 21: Finding the Best-Fit Transfer Function Parameters.

Figure 22 shows the RSS best-fit comparison between the simulation and hot-fire test data for a prescribed throttle profile corresponding to a pull-up push-over maneuver of the TGALS vehicle[xiv]. For this fit, the simulation best matched when $\{\tau_2 = 0.7 \text{ and } \zeta_2 = 1.9\}$.

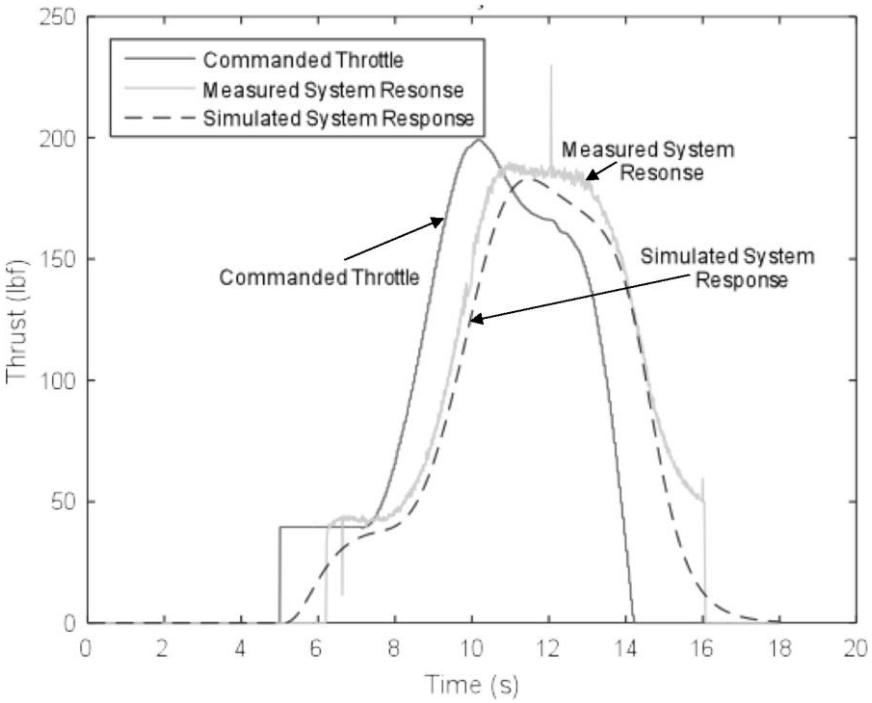

Figure 22: Simulation Compared to Hot-Fire Test for Given Commanded Throttle Profile, $\{\tau_2 = 0.7 \text{ and } \zeta_2 = 1.9\}$.

Using this transfer function parameter set for the ballistic model, various values of the control law parameter set $\{\omega_p \text{ and } k_p\}$ were evaluated, and allowed the control law to be tuned for a best system response. Figure 23 shows a sample of various simulation runs and illustrates the effects of the control law parameter set. These simulation results were verified through follow-on hot fire test, the results of which are shown in Figure 24.

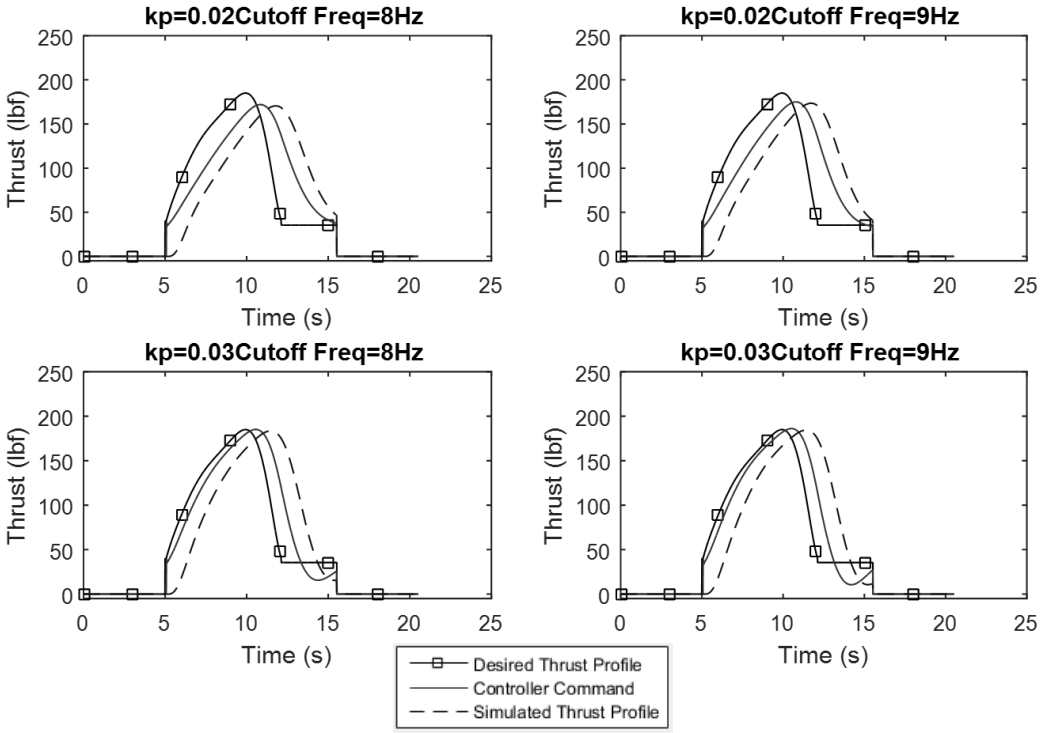

Figure 23: Sample Controller Tuning Simulation Runs.

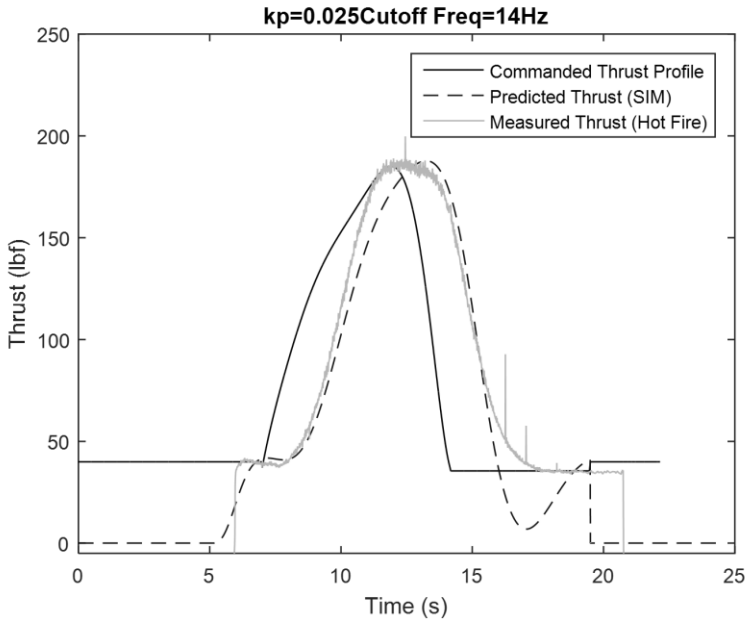

Figure 24: Verification Push-up Pull-over Thrust Profile

V. Conclusion

This document presents a status update of the design and integration of a throttled launch assist hybrid rocket motor for an airborne nano-launch platform. Currently, NASA Armstrong Flight Research Center (AFRC) is developing a scaled prototype of a high lift-to-drag (L/D) ratio glider designed as a flexible low earth orbit (LEO) launch platform for nano-scale satellites (NanoSats). Because the high L/D platform is delivered to the launch altitude and airspeed using a high-efficiency air-breathing propulsion system, there is a significant reduction in the required ΔV that must be delivered by the launch vehicle. Optimal ΔV savings are achieved when the NanoSat launch vehicle is delivered to a high-flight path angle that will approximate the condition that would be achieved along a ground launch trajectory at the same altitude and airspeed.

The glider platform itself is unable to achieve this flight condition, and launch assist propulsion is required. A hybrid system was selected for the launch assist motor because of the inherent safety, operational simplicity, and environmental friendliness of the propellants; and because of the ability for the hybrid system to be throttled and restarted on demand. This study establishes the requirements for this launch assist propulsion system, develops the system design features, presents the end-to-end hardware layout, develops the closed-loop throttle control law, develops the simulation used to tune control parameters, and shows the result of hot fire when using the best picked closed loop controller parameters.

A closed loop, proportional control system is utilized to generate a voltage output command for throttling purposes. An option to have a second order Butterworth filter to smooth the output voltages is available. Options for user-prescribed thrust profile inputs are available, including step, ramp, and pull-up push-over maneuver. Values for the proportional gain k_p the lowpass filter cutoff frequency ω_p, are user selectable. A medium fidelity motor simulation is derived from

preliminary ground test data and is used to tune the parameters of the closed-loop control law without having to perform multiple hot-fire tests.

Initial static tests were performed with a cylindrical fuel port to verify system functionality and establish a baseline for the propellant regression rate and optimal O/F ratio. Subsequent tests are performed using a helical fuel port to increase the volumetric efficiency of the system and allow operation near the optimal oxidizer-to-fuel condition. Multiple restarts of each system configuration are demonstrated. Results of both open and closed loop throttle tests are presented.

Static throttle tests were curve fit and used to generate look-up tables that correlate the servo command voltage to motor thrust and chamber pressure to motor thrust. Using these data tables, a proportional-gain, closed-loop controller using chamber pressure feedback was developed and implemented within the real-time code that resides on the controlling laptop computer. Closed loop system tuning has been completed for the current iteration of the ground test. Follow-on work will consist of integrating the system onto the glider pylon and modifying the control code for the chosen flight computer. Ground testing for the integrated system will be performed, and once any remaining safety checks have been passed, the system will be ready for flight.

References

[i] Bartolotta, Paul, Wilhite, Alan W., Schaeffer Mark, Voland, Randall T., and Huebner, Larry, " Horizontal Launch: A Versatile Concept for Assured Space Access," NASA/SP-2011-21599, December 2011.

[ii] Lanre, A. M., Fashanu, T. A., and Osheko, A. C., " Parameterization of Micro Satellite Launch Vehicle," J. Aeronautics and Aerospace Engineering, Vol. 3, No. 2, February 2014., http://dx.doi.org/10.4172/2168-9792.100013.

[iii] Hague, N. Capt., Siegenthaler, Erika, Lt. Rothman, Julia, "Enabling Responsive Space: F-15 Microsatellite Launch Vehicle", AIAA J. of Spacecraft and Rockets, IEEEAC paper # 1102, December 2002, https://wiki.umn.edu/pub/AEM_Air_Launch_Team/Aircraft/Enabling_responsive_space-F-15_microsatellite_launch_vehicle.pdf

[iv] Chen, T. T., Ferguson, P. W., " Responsive Air Launch Using F-15 Global Strike Eagle," RS4-2006-20014th Responsive Space Conference, Los Angeles CA, April 24-27, 2006,

[v] Stephen A. Whitmore, Sean D. Walker, Daniel P. Merkley, and Mansour Sobbi. "High Regression Rate Hybrid Rocket Fuel Grains with Helical Port Structures", AIAA J. Propulsion and Power, Vol. 31, No. 6 (2015), pp. 1727-1738.

[vi] Stephen A. Whitmore, Nathan Inkley, and Daniel P. Merkley, "Development of a Power-Efficient, Restart-Capable Arc Ignitor for Hybrid Rockets", *AIAA J. Propulsion and Power*, Vol. 31, No. 6 (2015), pp. 1739-1749.

[vii] Anon., "Department of Defense Interface Standard, Electromagnetic Environmental Effects Requirements for Systems," MIL-STD-464, http://www.tscm.com/MIL-STD-464.pdf [Retrieved 8 October 2014].

[viii] Anon., "High Power 8C-30C Series, Single Output High Voltage DC/DC Modules," UltraVolt, Inc., *http://www.ultravolt.com/uv_docs/HP8C-30CDS.pdf*, [Retrieved 9 October 2014].

[ix] Whitmore, S. A., Merkley, S. L., Walker, S. D., Tonc, L., Spurrier, Z. S., and Mathias, S., "Survey of Selected Additively Manufactured Propellants for Arc-Ignition of Hybrid Rockets," AIAA 2015-2616, *51st AIAA/ASME/SAE/ASEE Joint Propulsion Conference and Exhibit*, Orlando FL, 27-29 July, 2015.

[x] Whitmore, Stephen A., Peterson, Zachary W., and Eilers, Shannon D., "Comparing Hydroxyl Terminated Polybutadiene and Acrylonitrile Butadiene Styrene as Hybrid Rocket Fuels," AIAA J. Propulsion and Power, vol. 29, no. 3, May–June 2013.

[xi] Sutton, G. P., and Biblarz, O., Rocket Propulsion Elements, 7th ed., Wiley, New York, 2001, Chaps 4-5.

[xii] Gordon, S., and McBride, B. J., "Computer Program for Calculation of Complex Chemical Equilibrium Compositions and Applications," NASA RP-1311, 1994.

[xiii] Arif Karabeyoglu, "Lecture 10 Hybrid Rocket propulsion Design Issues," AA 284a Advanced Rocket Propulsion, AAE Department, Stanford University, May 14, 2012, p. 18, http://www.spg-corp.com/docs/Stanford_AA284a_Lecture10.pdf, [Retrieved 01 January, 2016].

[xiv] Whitmore, Stephen A., Merkley, Stephen L., Walker, Sean D., and Spurrier, Zachary S. "Throttled Launch-Assist Hybrid Rocket Motor for an Airborne NanoSat Launch Platform", 51st AIAA/SAE/ASEE Joint Propulsion Conference, Propulsion and Energy Forum, (AIAA 2015-3940), 28-30 July 2015, http://dx.doi.org/10.2514/6.2015-3940.